Mechanical Ball Milling Introducing Ti Particles to Accelerate Gas Nitriding of 42CrMo Steel: Microstructure and Tribological Properties

Yulong Zhou , Hui Zhang , Yuan Yao , Yubo Zhang , Haoping Peng , Jianhua Wang * , Zhiwei Li *

Posted Date: 27 May 2026

doi: 10.20944/preprints202605.1901.v1

Keywords: mechanical ball milling; gas nitriding; growth kinetics of nitrided layer; friction and wear

 doi:10.20944/preprints202605.1901.v1

Article

Mechanical Ball Milling Introducing Ti Particles to Accelerate Gas Nitriding of 42CrMo Steel: Microstructure and Tribological Properties

Yulong Zhou [1], Hui Zhang [1], Yuan Yao [1], Yubo Zhang [2], Haoping Peng [1,2], Jianhua Wang [2,*] and Zhiwei Li [1,2,*]

[1] School of Materials Science and Engineering, Changzhou University, 213164, Jiangsu, P.R. China.

[2] School of Petroleum and Natural Gas Engineering, Changzhou University, 213164, Jiangsu, P.R. China.

* Correspondence: wangjh@cczu.edu.cn (J.W.); lzw@cczu.edu.cn (Z.L.)

Abstract

The rolling ball mill and the Lab-Nit gas nitriding furnace were employed to investigate the effects of mechanical ball milling pretreatment with Ti particle incorporation on the gas nitriding efficiency and nitrided layer properties of 42CrMo steel. The results show that ball milling impact creates pit defects on the steel surface, providing mechanical anchoring sites for Ti powder particles to achieve uniform fixation of Ti on the substrate surface. The nitrided layer consists of a loose surface layer and a compact subsurface layer, both dominated by the Fe_4N phase. After 40 min of mechanical ball milling pretreatment with Ti particle incorporation, the total thickness of the nitrided layer increases by 42.0% compared with the untreated sample, and the proportion of the loose layer decreases to 16.9%. In contrast, 40 min of pure ball milling pretreatment only increases the total thickness by 12.0%, with the loose layer proportion reaching 23.2%. The hardness enhancement induced by Ti particle incorporation is mainly concentrated in the loose layer. Pure ball milling has no significant effect on the hardness of the loose layer (525±3 HV), while the loose layer hardness increases stepwise with treatment time after mechanical ball milling with Ti particle incorporation, reaching 550±2 HV after 40 min of pretreatment. Nanoindentation tests reveal that the surface nanohardness of the BM2+Ti+N4 sample reaches 5.43 GPa, an increase of approximately 5%–6% compared with the untreated and pure ball-milled samples. The wear rate decreases to 1.20×10^{-8} $mm^3/N\cdot m$, a reduction of 78% compared with the pure ball-milled sample. The in-situ formation of the TiN compound layer fills surface micropores and strengthens the surface shear resistance.

Keywords: mechanical ball milling; gas nitriding; growth kinetics of nitrided layer; friction and wear

1. Introduction

Gas nitriding can produce a high-hardness, wear-resistant, and fatigue-resistant surface at low temperatures without quenching distortion, and has become the final surface strengthening process for key components such as wind power bearings, gears, and crankshafts [1-3]. However, according to the Fe-N phase diagram [4], the diffusion coefficient of nitrogen in α-Fe below 590 °C is only about $10^{-11}\cdot m^2\cdot s^{-1}$. To obtain a hardened layer with a depth of tens of micrometers, industrial holding often takes 30–80 h, leading to high energy consumption, slow production cycles and large furnace occupancy. Especially for large rings of wind turbines above 5 MW, the single-piece nitriding cycle can exceed 72 h, which seriously restricts the promotion of green manufacturing.

To shorten the process time, researchers have proposed acceleration strategies such as plasma nitriding, surface mechanical attrition, and trace element catalysis. Plasma nitriding uses cathode sputtering to generate high-density active nitrogen atoms, which can increase the growth rate of the nitrided layer by 2–3 times [5-6]. However, its discharge uniformity imposes higher tooling requirements for ultra-large/overweight workpieces, and the maintenance cost of cathode power

 doi:10.20944/preprints202605.1901.v1

supplies and vacuum systems is high. In contrast, gas nitriding furnaces have a simple structure, low investment, and are easy to realize large-scale well-type or bell-type structures, making them more suitable for batch processing of 100-meter-level wind power rings or dozens of tons of heavy-duty gear shafts, thus still dominating the production of ultra-large parts. Surface mechanical treatment (sandblasting, ball milling, etc.) increases the density of nitrogen diffusion channels by refining grains and introducing vacancies. Although simple and independent of part size, this treatment increases surface roughness, which tends to produce an excessively thick loose layer in the initial nitriding stage, consequently degrading the density and fatigue resistance of the nitrided layer [7–9]. Trace element catalysis relies on the high affinity of Ti, Al, Cr, and other elements for nitrogen to form M-N compounds in-situ on the surface, increasing the local nitrogen potential and reducing the diffusion activation energy. However, traditional electroplating or spraying requires high-temperature melting or post-solution treatment, which not only increases energy consumption but also may cause pollution [10-12]. It is still a challenge to quantitatively and uniformly introduce trace catalytic elements on large-area curved surfaces.

Ti is considered an ideal element for catalyzing nitriding due to its high nitrogen affinity and low diffusion activation energy, but existing work is mostly limited to ion implantation or Ti foil encapsulation, which are restricted by sample size and costly. On the other hand, high-energy ball milling has been proven to mechanically embed Al, Ti, and other powders onto the steel surface at room temperature, forming a mechanically alloyed layer with a thickness of several micrometers and uniform particle distribution [13-15]. Nevertheless, studies directly coupling mechanical ball milling with Ti particle incorporation and subsequent gas nitriding remain scarce, particularly regarding systematic investigations of Ti active site effects on nitriding kinetics and nitrided layer quality. Quantitative data for 42CrMo high-strength steel, a critical shaft material, are especially lacking.

This study proposes a one-step method of introducing Ti particles via mechanical ball milling: high-energy collision of ZrO_2 grinding balls in a rolling ball mill is used to quantitatively embed 200-mesh pure Ti powder onto the surface of quenched and tempered 42CrMo steel, followed by direct transfer to a conventional gas nitriding furnace for nitriding at 520 °C for 4 h. This scheme requires no additional heating or coating equipment, and can construct Ti active sites on the workpiece surface to achieve rapid nitriding. Systematic characterization of nitrided layer thickness, loose layer proportion, phase composition, hardness gradient, and wear performance elucidates the coupling mechanism of Ti nanoparticles with both nitriding growth kinetics and surface tribological behavior, providing new insights into efficient and sustainable low-temperature nitriding.

2. Experimental Methods

2.1. Sample Preparation

The 42CrMo steel used in this study was derived from hot-rolled normalized steel plate, and its main chemical composition is shown in Table 1. The 42CrMo steel plate was cut into 150 mm×40 mm×40 mm blanks by wire cutting, oil-quenched at 840 °C for 30 min, and tempered at 560 °C for 2 h. The microstructure and phase composition after quenching and tempering are shown in Figure 2. The results show that the treated sample exhibits an α-Fe phase. It was then processed into 10 mm×10 mm×5 mm test pieces, the surfaces were gradually polished with 400, 800, and 1200-mesh SiC water sandpapers, ultrasonically cleaned with anhydrous ethanol for 5 min, and dried with cold air for later use.

Table 1. Nominal chemical composition of 42CrMo steel (wt.%).

C	Si	Mn	Mo	Cr	Fe
0.38–0.45	0.2–0.4	0.5–0.8	0.15–0.25	0.9–1.2	Bal.

Table 2 lists the sample designations and corresponding process parameters. For ease of analysis, the ball milling group without Ti powder addition was set as the control group. The ball milling process (BM) placed 42CrMo steel plates together with ZrO_2 grinding balls at a volume percentage

 doi:10.20944/preprints202605.1901.v1

of 20% in a ball milling tank. The volume percentage refers to the proportion of grinding balls to the total volume of the ball milling tank. The grinding tank has a diameter of 60 mm and a height of 60 mm. The rolling speed was 120 r/min, and the grinding times were 20 min, 40 min, 60 min, and 80 min, respectively. The samples were marked as BM(1, 2, 3, 4).

The pretreatment process of introducing Ti particles via mechanical ball milling (BM+Ti) was as follows: 42CrMo steel plates, ZrO_2 grinding balls at a volume ratio of 20%, and Ti powder at a volume ratio of 10% were placed in a ball milling tank, and the pretreatment times were 20, 40, 60, and 80 min, respectively, as shown in Figure 1(a). The Ti powder used had a purity of 99.99 wt.% and a particle size of 200 mesh. The samples were marked as BM(1, 2, 3, 4)+Ti. The adhesion amount of Ti powder was measured by the weight difference of the samples before and after pretreatment, and the results are shown in Table 3.

The gas nitriding process (N) was carried out in a Lab-Nit gas nitriding furnace [16]. The equipment operates at a voltage of 380 V, a frequency of 50 Hz, and a heating power of 4 kW. Figure 1(b) details the nitriding process parameters. The samples were placed in the reaction chamber of the furnace, and the temperature was gradually raised from 25 ℃ to 520 ℃ under a nitrogen atmosphere. After reaching 520 ℃, NH_3 gas was introduced into the reaction chamber to start nitriding. After the treatment was completed, heating was stopped, and N_2 gas was introduced to assist cooling. When the furnace temperature dropped to approximately 150 ℃, gas introduction was stopped, and the system was naturally cooled to room temperature.

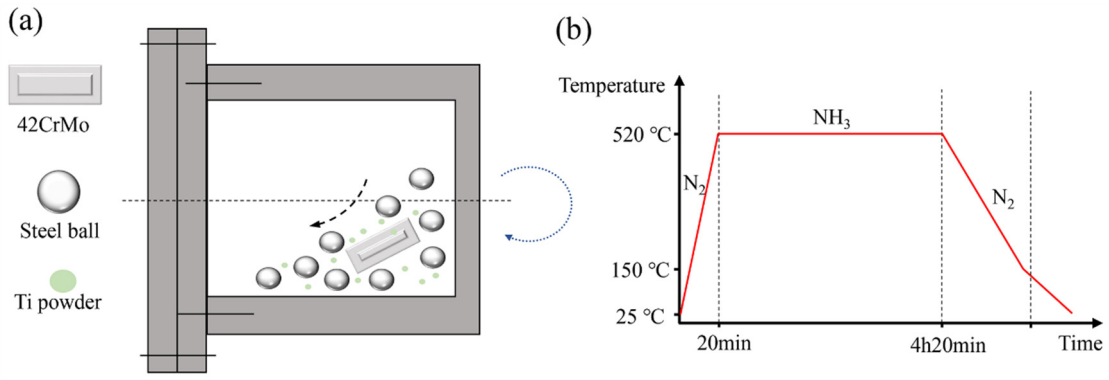

Figure 1. (a) Schematic diagram of pretreatment by introducing Ti particles via mechanical ball milling; (b) Temperature and gas flow program of gas nitriding.

Table 2. Sample designations and corresponding process parameters.

Sample designation	Process parameters
BM(1,2,3,4)-42CrMo	Ball milling pretreatment, time: 20 min, 40 min, 60 min, 80 min
BM(1,2,3,4)+Ti	Pretreatment by introducing Ti particles via mechanical ball milling, time: 20 min, 40 min, 60 min, 80 min
BM(1,2,3,4)+N4	Ball milling pretreatment + 4 h gas nitriding
BM(1,2,3,4)+Ti+N4	Pretreatment by introducing Ti particles via mechanical ball milling + 4 h gas nitriding

Table 3. Adhesion amount of Ti powder on the substrate surface after BM+Ti pretreatment for different times /mg.

Sample	Pretreatment time /min	Ti powder adhesion amount /mg
BM1+Ti	20	1.02±0.21
BM2+Ti	40	1.82±0.37
BM3+Ti	60	2.10±0.25
BM4+Ti	80	2.35±0.31

 doi:10.20944/preprints202605.1901.v1

2.2. Microstructure and Phase Analysis

The nitrided samples were cut along the center by wire cutting and embedded, then the cross-section was polished to the mirror finish. After polishing, 4% nitric acid-alcohol solution was used as an etchant for etching, followed by rinsing with alcohol, drying, and sample preparation.

A scanning electron microscope (SEM, model JSM-6510) was used to observe the surface and cross-sectional morphology of the nitrided layer of 42CrMo steel, with an accelerating voltage of 20 kV, a working distance of 8.0 mm, an X-ray imaging resolution of 1024×768 pixels, and an analysis depth of approximately 1 μm.

After gas nitriding, phase analysis of the nitrided surface layer was performed. The equipment used was an Ultima IV X-ray diffractometer equipped with a Cu target, a scanning voltage of 40 kV, a scanning current of 40 mA, a scanning angle of 10° to 90°, and a scanning rate of 5°/min.

An X-ray photoelectron spectrometer (XPS, Thermo Scientific K-Alpha) with a monochromatic Al X-ray source was used to analyze the surface of nitrided samples to study Ti elements [17], at an energy of 1486.6 eV, a voltage of 15 kV, and a power of 200 W. Measurement data and high-resolution core level spectra of C and Ti elements were collected. The C1s line at 284.8 eV was used as the absolute binding energy normalization benchmark. XPS spectrum analysis was completed using Thermo Avantage software (version 5.967).

Ti-enriched areas on the surface of the nitrided layer samples were determined by SEM imaging. A W/C protective layer was deposited under 30 kV and 1 nA electron beam conditions. A FEI Scios 2 HiVac focused ion beam was used to cut Ti-rich embryos from the surface of the nitrided layer and transfer the embryos to a copper grid. The samples were then thinned sequentially with focused ion beams at 30 kV, 4 nA, 1 nA, 0.3 nA, and 0.1 nA until the thickness reached 50–70 nm. A Tecnai G2 F20 S-Twin transmission electron microscope was used to observe the cross-sectional microstructure of Ti-rich embryos at an accelerating voltage of 200 kV.

2.3. Performance Testing

The substrate surface roughness was measured using a TR200 handheld roughness meter, calculated as *Ra* value according to ISO 4287, with 5 points measured per sample and the average taken. *Ra*, as the arithmetic mean deviation of the profile, can equivalently reflect the average depth of ball milling pits; the opening width of the pits was not quantitatively counted and was directly observed by SEM morphology.

The surface hardness of the samples and the cross-sectional hardness of the nitrided layer were measured using an HVS-30P digital Vickers hardness tester with a load of 0.2 kgf and a holding time of 10 s. To detect the hardness gradient change of the samples from the surface to the core, hardness measurements were performed at intervals along the direction from the surface to the core. At each measurement point, three points were taken along the vertical direction for hardness measurement, and the average value was taken as the hardness value of that position.

Nanoindentation tests of the nitrided layer surface were performed using a Hysitron TI 950 tester with a Berkovich triangular diamond indenter and a maximum load of 9 mN. The loading and unloading processes took 1 s. The surface nanohardness of the nitrided layer was obtained from the load-displacement fitting curve automatically recorded by the system.

Dry sliding wear tests were completed on a ball-on-disk tribometer, with an HRC 62 GCr15 steel ball as the counterpart, a load of 5 N, a rotating speed of 200 rpm, a linear speed of 0.1 m s^{-1}, a time of 30 min, a total stroke of 180 m, an ambient temperature of 23 °C, and a relative humidity of 45%±5%. The wear scar profile was scanned by a white light interferometer, and the volumetric wear rate was calculated by the area integration method, with three averages. The friction coefficient collection frequency was 100 Hz, and the steady-state average value from 5–25 min was taken.

 doi:10.20944/preprints202605.1901.v1

3. Results and Discussion

3.1. Microstructure Evolution

As shown in Figure 2(a), the surface of untreated 42CrMo steel is smooth and flat, and its microstructure consists of fine and uniform martensite and retained austenite. Figure 2(b) shows the microstructure of 42CrMo steel surface after 40 min of ball milling treatment, where the black areas are depressions formed on the steel substrate surface by mechanical collision during ball milling. Figure 2(c) presents the microstructure of 42CrMo steel surface after 80 min of ball milling treatment, and the black areas increase significantly. The roughness tester results show that the surface roughness *Ra* of BM2 sample is 0.67±0.15 μm, and that of BM4 sample is 0.72±0.12 μm. It can be seen that prolonging the ball milling time has no significant effect on the surface roughness value of the steel substrate, because the roughness is determined by the particle size of the grinding steel balls. When the particle size of the grinding steel balls is constant, the surface roughness of the substrate will stabilize within a certain range. Compared with Figure 2(b), the area fraction of black areas on the steel substrate surface after BM4 treatment increases, indicating that prolonging the ball milling time can increase the depression area on the steel substrate surface. Figure 2(d) shows the X-ray diffraction patterns of 42CrMo steel after different grinding times, and it can be seen that only the α-Fe phase exists on the substrate surface, and the ball milling process has no effect on the phase composition of the substrate surface.

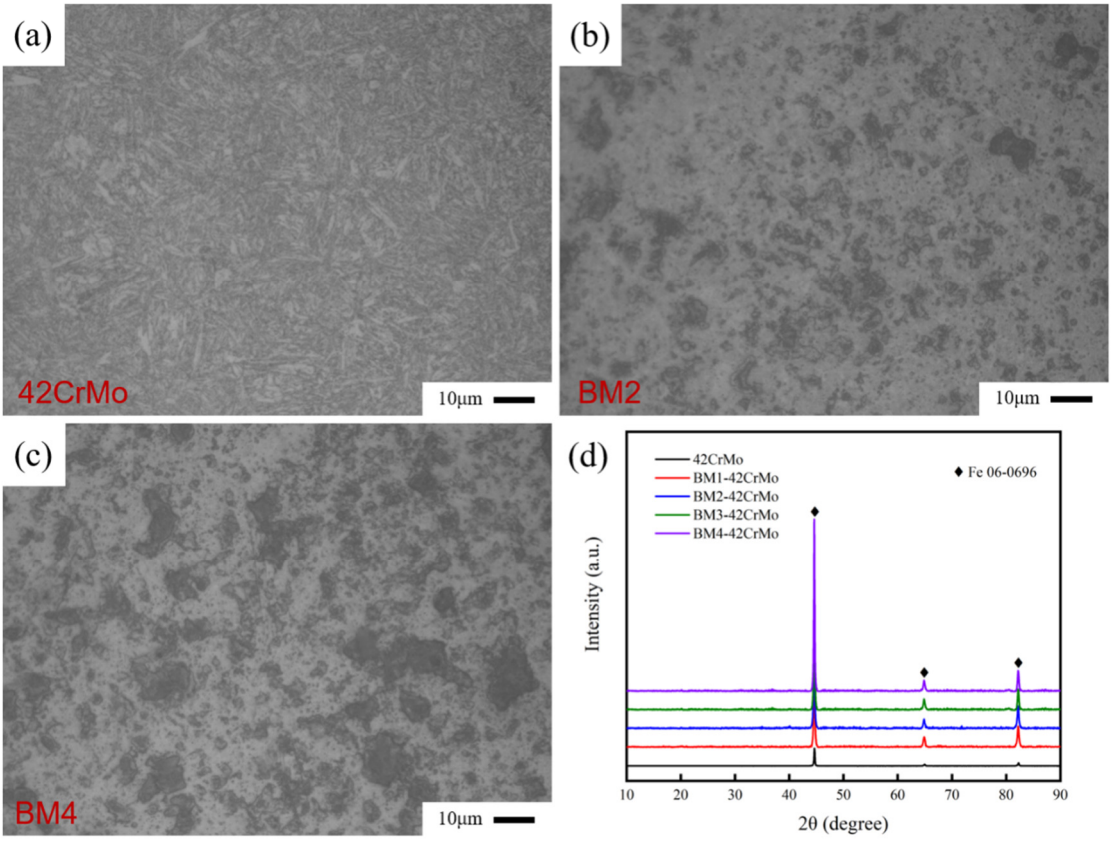

Figure 2. Surface micromorphology of 42CrMo steel: (a) Untreated; (b) Ball milled for 40 min; (c) Ball milled for 80 min; (d) X-ray diffraction patterns of 42CrMo steel surface after different ball milling times.

Figures 3(a) and (b) show that after BM+Ti treatment, granular Ti is distributed on the steel substrate surface, and the number of particles increases with the prolongation of treatment time. Figure 3(c) presents the X-ray diffraction patterns of the substrate surface after different treatment times, and it can be seen that Ti element diffraction peaks appear on the substrate surface after BM+Ti

 doi:10.20944/preprints202605.1901.v1

treatment [21]. Figure 3(d) is a micro-area enlarged photo of the granular substance in Figure 3(b), and it can be seen that the main component of the granular substance is Ti. This indicates that after BM+Ti treatment, Ti powder is fixed on the substrate surface in granular form, because the pits formed on the substrate surface by ball milling become the fixation sites of Ti powder. Table 3 shows the adhesion amount of Ti powder on the substrate surface after BM+Ti treatment for different times. After BM1+Ti treatment, the Ti powder adhesion amount on the sample surface is 1.02±0.21 mg; after BM2+Ti treatment, the adhesion amount reaches 1.82±0.37 mg, an increase of 78% compared with BM1+Ti sample. When the treatment time is extended from 20 min to 40 min, the surface Ti powder adhesion amount increases significantly. After the treatment time reaches 40 min, the growth of surface Ti powder adhesion amount tends to be gentle.

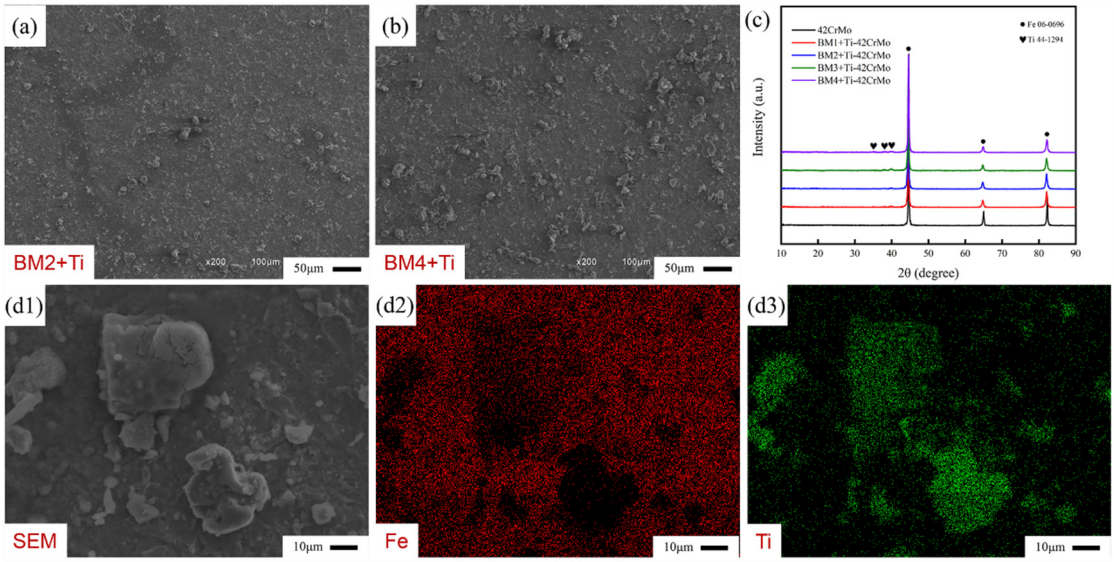

Figure 3. Substrate surface micromorphology after BM+Ti pretreatment for 40 min (a) and 80 min (b); (c) X-ray diffraction patterns of sample surfaces after different pretreatment times; (d1) magnified view of the region indicated in Figure (b); (d2) Fe element distribution map in Figure (d1); (d3) Ti element distribution map in Figure (d1).

Figure 4. a-c) show the cross-sectional secondary electron images of untreated, BM2, and BM4 samples after N4 treatment, respectively, and Figure 4(d) presents the X-ray diffraction patterns of the corresponding sample surfaces. After 4 h of nitriding treatment, the surface of the nitrided layer is uneven and covered with irregularly distributed black pores, defined as the loose layer; the subsurface of the nitrided layer is uniform and flat, defined as the compact layer. It can be seen that the nitrided layer is composed of two parts: a loose layer and a compact layer. X-ray diffraction patterns show that the nitrided layer is composed of Fe_4N [22], indicating that the loose layer and the compact layer belong to the same Fe_4N phase, with only microstructural differences. As shown in Figure 4(a), the loose layer in the nitrided layer of the untreated sample is thin; as shown in Figure 4(b), the nitrided layer thickness of the BM2 sample increases, and the loose layer thickness also increases; as shown in Figure 4(c), the loose layer of the BM4 sample further thickens, occupying nearly half of the total nitrided layer thickness. It can be seen that with the extension of ball milling time, the total nitrided layer thickness shows an increasing trend; ball milling treatment can thicken the loose layer in the nitrided layer, and the longer the ball milling time, the greater the loose layer thickness.

 doi:10.20944/preprints202605.1901.v1

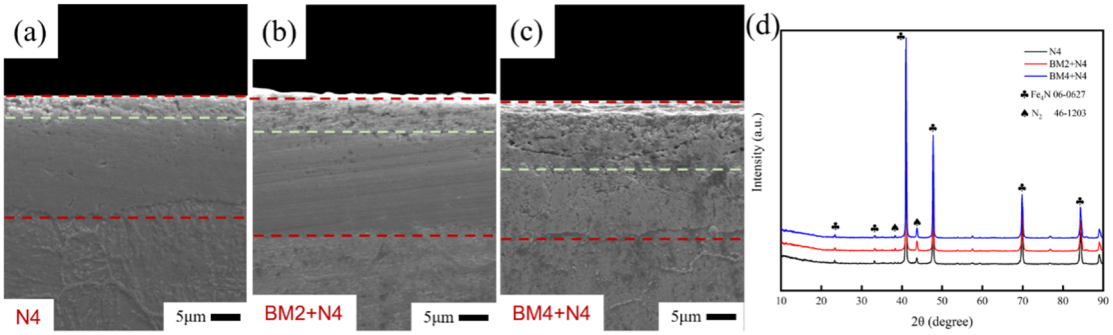

Figure 4. Cross-sectional secondary electron micrographs of 42CrMo steel after 4 h of gas nitriding treatment after different ball milling times: (a) Untreated sample; (b) Ball milled for 40 min; (c) Ball milled for 80 min; (d) X-ray diffraction patterns of 42CrMo steel surface after 4 h of gas nitriding treatment after different ball milling times.

Figure 5 shows the cross-sectional secondary electron micrographs of BM1+Ti+N4, BM2+Ti+N4, and BM4+Ti+N4. After 4 h of gas nitriding, the nitrided layer is also composed of a loose layer and a compact layer. With the extension of BM+Ti treatment time, the total thickness of the nitrided layer increases. Compared with the BM+N4 series, the proportion of loose layer in the nitrided layer of the BM+Ti+N4 series decreases. Moreover, the loose layer thickness does not show a significant change trend with the extension of treatment time.

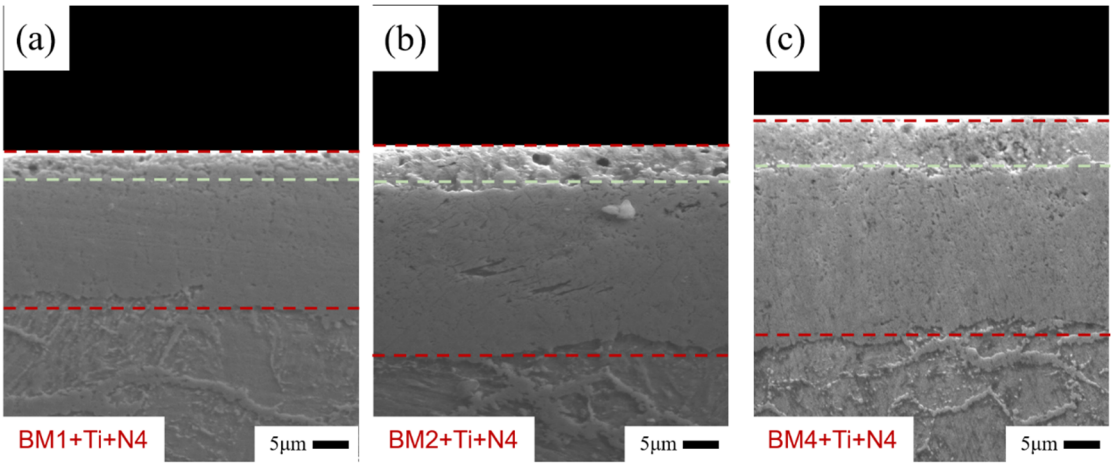

Figure 5. Cross-sectional secondary electron micrographs of 42CrMo steel after 4 h of gas nitriding treatment after different BM+Ti pretreatment times: (a) 20 min; (b) 40 min; (c) 80 min.

3.2. Growth Kinetics

Figure 6(a) shows the statistics of nitrided layer thickness of untreated, BM2, and, BM4 samples after 4 h of gas nitriding. The total nitrided layer thickness of the untreated sample is 20.8 μm, including a loose layer of 4.1 μm, accounting for 19.9%; the total thickness of BM2 is 23.3 μm, and the loose layer thickness is 5.4 μm; the total thickness of BM4 is 23.7 μm, and the loose layer thickness is 11.2 μm, with the proportion rising to 47.3%. It can be seen that with the extension of ball milling time, the total nitrided layer thickness increases slowly, while the proportion of loose layer expands linearly.

Figure 6(b) shows the results of the BM+Ti+N4 series. The total thickness of BM1+Ti+N4 is 22.0 μm, and the loose layer accounts for 16.8%; the total thickness of BM2+Ti+N4 is 29.5 μm, and the loose layer accounts for 16.9%; the total thickness of BM4+Ti+N4 is 30.0 μm, and the loose layer accounts for 19.4%. Compared with BM1+Ti+N4, the total thickness of BM2+Ti+N4 increased by 34%, while the loose layer proportion remained below 20%, confirming that mechanical ball milling with

 doi:10.20944/preprints202605.1901.v1

Ti particle incorporation accelerates nitrided layer growth while effectively suppressing excessive loose layer thickening.

According to the parabolic growth law, the rate constant $k = d^2/t$ (d is the total layer thickness, t is time) for nitriding at 520 °C for 4 h. The k value of the untreated sample is 1.3×10^{-2} μm² min⁻¹, which is consistent with the nitrogen diffusion coefficient in α-Fe reported in the literature [18], and the loose layer proportion is 19.9%. The total layer thickness of BM2+N4 is 23.3 μm, corresponding to k = 1.5×10^{-2} μm² min⁻¹, with a limited increase and the loose layer proportion rising to 23.2%; the k value of BM2+Ti+N4 rises to 2.6×10^{-2} μm² min⁻¹, an increase of about one time, indicating that the introduction of Ti particles significantly increases the nitrogen flux, and the loose layer proportion drops to 16.9%.

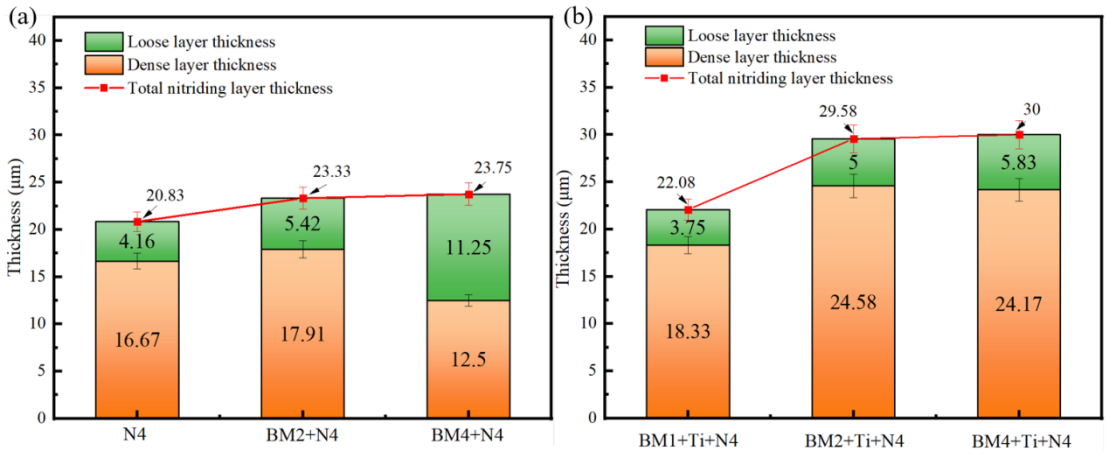

Figure 6. Nitrided layer thickness of samples after 4 h of gas nitriding under different pretreatments: (a) ball milling treatment for different durations; (b) mechanical ball milling with Ti particle incorporation pretreatment for different durations.

BM2+Ti+N4 was selected as a typical sample to analyze the microstructure of the nitrided layer, as shown in Figure 7. On the surface of the nitrided layer of the BM2+Ti+N4 sample, a blocky microstructure with low contrast appears. The element distribution map shows that the blocky structure is the Ti and N enrichment area [23], which is consistent with the results in Figure 3. The blocky structure enriched with Ti and N was cut out using focused ion beam technology. The cross-sectional microstructure is shown in Figure 7(b). It can be seen from the cross-section that the blocky structure is divided into three layers along the depth direction of the nitrided layer: the outermost layer has low contrast and is compact, mainly composed of Fe and N elements; the middle layer has high contrast, mainly composed of N and Ti elements; the innermost layer is loose and porous, composed of Fe and N elements. Combined with the results in Figures 5 and 6, it is speculated that the outermost layer is a compact Fe_4N layer, the middle layer is a TiN layer, and the innermost layer is a loose Fe_4N layer. The middle layer was further observed by HR-TEM (Figure 7(c)). Identified by diffraction (Figure 7(d)), the middle layer is composed of TiN compound. Pretreatment by introducing Ti particles via mechanical ball milling not only compensates for the defect of excessive loose layer thickness caused by ball milling treatment, but also increases the enrichment degree of nitrogen element on the surface of the nitrided layer. In addition, the formation of the TiN compound layer transforms the Ti powder physically attached to the substrate surface into chemical bonds [24], firmly fixed on the surface of the nitrided layer, thus ensuring the compactness and integrity of the nitrided layer.

 doi:10.20944/preprints202605.1901.v1

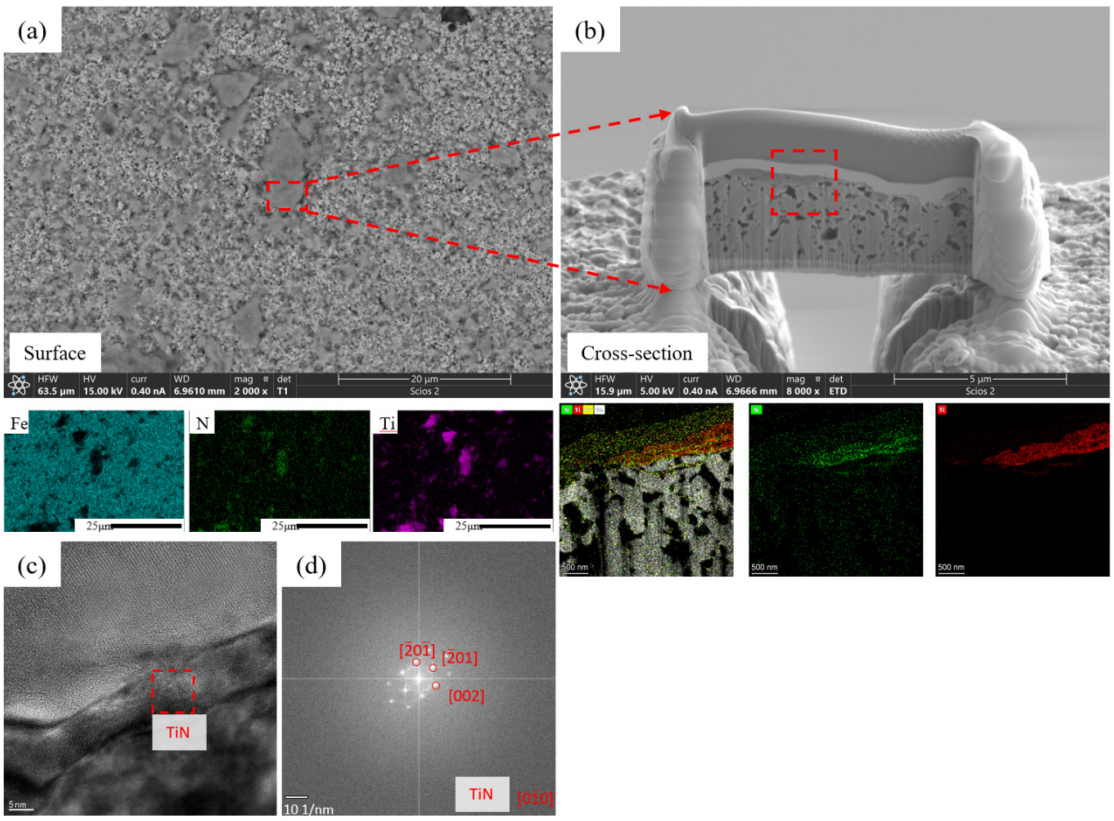

Figure 7. (a) Surface micromorphology of the nitrided layer and Fe, N, Ti element distribution maps in BM2+Ti+N4 sample; (b) cross-sectional micromorphology and Fe, N, Ti element distribution maps of Ti-rich area cut by FIB; (c) transmission electron microscope image of the middle TiN compound layer; (d) diffraction spot pattern of TiN compound layer.

Figure 8 shows the X-ray photoelectron spectra of 42CrMo steel samples after 4 h of gas nitriding under different pretreatment conditions. Referring to the *ref.* [19], the $Ti_2p_3/_2$ binding energy of TiN chemical state is determined to be 454.9 eV, and that of TiO_2 chemical state is 458.5 eV. As shown in Figure 8(b), no Ti-containing compounds are detected in the nitrided layer of BM+N4 samples; high-resolution Ti 2p spectra appear in the BM+Ti+N4 series, corresponding to TiN and TiO_2 chemical states [25]. Based on the sensitivity factor, the relative Ti content of the nitrided layer under different treatment times is obtained by XPS spectroscopy, and the results are shown in Table 4. The Ti content on the surface of BM1+Ti+N4 nitrided layer is 0.7±0.1 wt.%, of which TiN chemical state accounts for 19%, and the rest is TiO_2; the Ti content on the surface of BM2+Ti+N4 nitrided layer is 1.1±0.2 wt.%, an increase of 57% compared with BM1+Ti+N4; the Ti content on the surface of BM4+Ti+N4 nitrided layer reaches 1.3±0.2 wt.%, an increase of 85% compared with BM1+Ti+N4. The proportion of TiN chemical state in the three groups of samples is about 20%, and the rest is TiO_2 chemical state. BM+Ti treatment can introduce Ti powder into the nitrided layer. With the extension of BM+Ti treatment time, the Ti content on the surface of the nitrided layer continues to increase. The surface Ti content of BM2+Ti+N4 is increased by 57% compared with BM1+Ti+N4. Ti in the nitrided layer exists in two chemical states: TiN and TiO_2, with the atomic proportion of TiN being about 20%.

 doi:10.20944/preprints202605.1901.v1

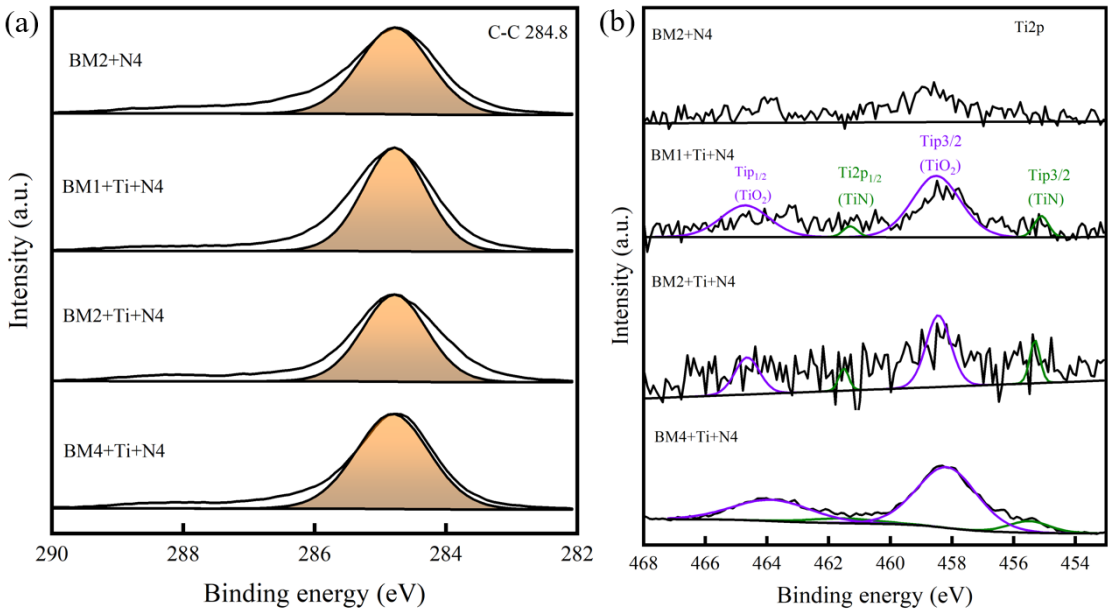

Figure 8. X-ray photoelectron spectra of 42CrMo steel samples after 4 h of gas nitriding under different pretreatment conditions: (a) C-C bond combination; (b) Ti bond combination.

Table 4. Ti content on the surface of nitrided layer of samples pretreated by introducing Ti particles via mechanical ball milling.

Sample	Surface Ti content (mass fraction)	Relative atomic content (atomic percentage)	
		TiN	TiO_2
BM1+Ti+N4	0.7±0.1	19%	81%
BM2+Ti+N4	1.1±0.2	19%	81%
BM4+Ti+N4	1.3±0.2	20%	80%

To intuitively describe the effect of pretreatment by introducing Ti particles via mechanical ball milling on the growth kinetics of gas nitriding, Figure 9 presents a schematic diagram of the mechanism. The mechanical effect of ball milling creates a large number of pits on the substrate surface, which become deposition sites for Ti powder particles. Therefore, pretreatment by introducing Ti particles via mechanical ball milling affects the growth kinetics of gas nitriding process mainly through the following two ways:

(1) Surface defects provide additional diffusion channels for nitrogen elements. During nitriding of untreated samples, surface Fe reacts with N to form Fe_4N and micropores, which become initial diffusion channels. However, with the formation of the compact subsurface nitrided layer, the inward diffusion of nitrogen atoms is hindered, resulting in a long time for gas nitriding. Ball milling pretreatment produces a large number of pit defects on the substrate surface, which become efficient channels for nitrogen diffusion, thus accelerating nitriding and thickening the nitrided layer. A loose layer with appropriate thickness can significantly promote nitriding kinetics. However, with the extension of ball milling time, the increase in the number of pits leads to an overly thick loose layer, and excessive nitrogen flows back to the external environment instead, making the nitriding efficiency unable to be further improved.

(2) Ti-N adsorption increases the nitrogen potential of the substrate surface. Ti powder particles fixed by ball milling become active sites for nitrogen atom adsorption, promoting nitriding kinetics according to the nitrogen potential difference principle [20]; meanwhile, Ti reacts with nitrogen to form TiN compound in-situ. The synergistic effect of increased nitrogen potential and TiN formation enables the BM+Ti+N4 sample to obtain a thicker nitrided layer than the pure ball-milled sample, and

 doi:10.20944/preprints202605.1901.v1

the loose layer thickness is significantly reduced. This is attributed to the Ti powder particles fixed in the pits filling the surface micropores, and the TiN and TiO_2 compounds densifying the loose layer.

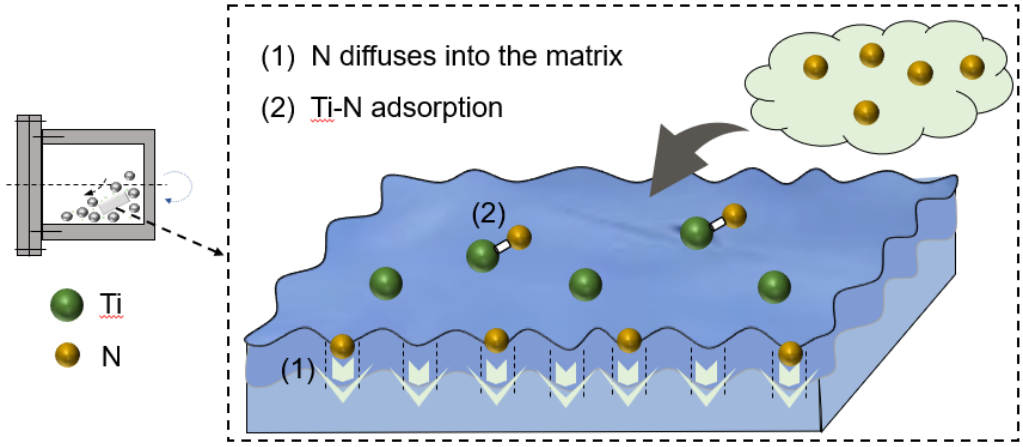

Figure 9. Mechanism of the effect of pretreatment by introducing Ti particles via mechanical ball milling on the growth kinetics of nitrided layer.

3.3. Friction and Wear

Figure 10 shows the hardness gradient line chart of the nitrided layer. The hardness of the compact layer of all samples is stable at 648±3 HV, much higher than the substrate hardness of 340±5 HV. The loose layer hardness of the BM+N4 series remains at 526±3 HV, while that of the BM+Ti+N4 series increases stepwise with pretreatment time. BM1+Ti+N4 is 525±3 HV, BM2+Ti+N4 rises to 550±2 HV, and BM4+Ti+N4 reaches 560±2 HV, an increase of 7.0%. The hardness increment is concentrated in the loose layer and is positively correlated with the content of TiN and TiO_2. When the surface Ti content of BM2+Ti+N4 is 1.1 wt%, the loose layer hardness increases by 4.8%, and when the Ti content of BM4+Ti+N4 is 1.3 wt%, it increases by 6.7%, confirming the strengthening effect of Ti compounds on the loose layer.

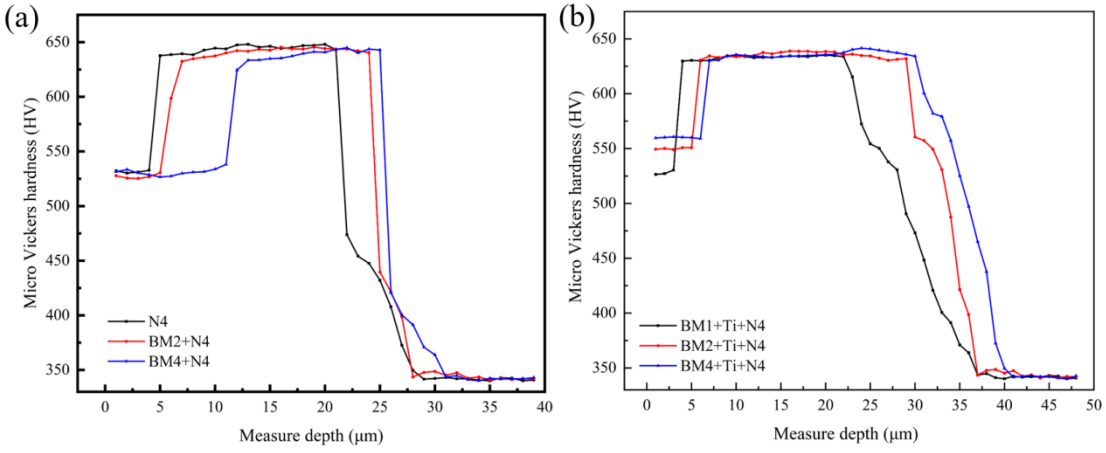

Figure 10. Hardness change curve with nitrided layer depth: (a) Nitrided samples pretreated by BM for different times; (b) nitrided samples pretreated by BM+Ti for different times.

N4, BM2+N4, and BM2+Ti+N4 were selected to further analyze the hardness and tribological properties of the loose layer. Figure 11 shows the distribution map of surface damage depth of the nitrided layer after friction and wear. Table 5 lists the performance parameters of friction and wear and nanoindentation. The average wear depth of N4 sample is 2.6 μm, and the wear rate reaches 3.74×10^{-8} $mm^3/N\cdot m$. After ball milling treatment, the average wear depth of BM2+N4 sample

 doi:10.20944/preprints202605.1901.v1

increases to 3.8 μm, and the wear rate rises to 5.35×10^{-8} mm³/N·m. Ball milling treatment will form pit defects on the substrate surface. During gas nitriding, surface defects provide more diffusion channels for nitrogen atoms, promoting the rapid growth of the nitrided layer [26]. However, this also leads to an overly thick loose layer of the nitrided layer, thereby increasing the wear depth and wear rate. After pretreatment by introducing Ti particles via mechanical ball milling, the average wear depth of BM2+Ti+N4 sample decreases to 2.3 μm, and the wear rate drops to 1.20×10^{-8} mm³/N·m. The Ti particles added during ball milling compensate for the pit defects caused by ball milling. As an active adsorption element, Ti powder increases the nitrogen potential of the sample surface and accelerates the growth of the nitrided layer [27]. At the same time, the formation of the TiN compound layer transforms the physically attached Ti powder into chemical bonding, further enhancing the surface wear resistance of the sample.

Nanoindentation tests show that the nanohardness of N4 and BM2+N4 samples is equivalent. The average nanohardness of BM2+Ti+N4 sample reaches 5.43 GPa, an increase of 5.03% compared with N4 sample and 6.26% compared with BM2+N4 sample, indicating that the formation of the TiN compound layer significantly improves the surface nanohardness of the sample, thereby enhancing the wear resistance of the BM2+Ti+N4 sample. It can be seen from Figure 7 that a continuous TiN polycrystalline layer is formed on the surface of the BM2+Ti+N4 sample, and the nanohardness of the TiN-enriched area reaches 11.81 GPa. This result is consistent with the XPS measurement result of Ti content on the surface of BM2+Ti+N4 sample in Figure 8, further confirming the strengthening effect of TiN phase. The wear scar morphology changes from wide and deep plough grooves to fine scratches, and the wear mechanism changes from oxidative-adhesive wear to slight abrasive wear [28]. In summary, pretreatment by introducing Ti particles via mechanical ball milling synergistically fills pits and strengthens with TiN nanobelts, improving the loose layer hardness, and significantly reducing the wear rate on the premise of keeping the compact layer hardness unchanged, realizing the quantitative optimization of the wear resistance of the nitrided layer.

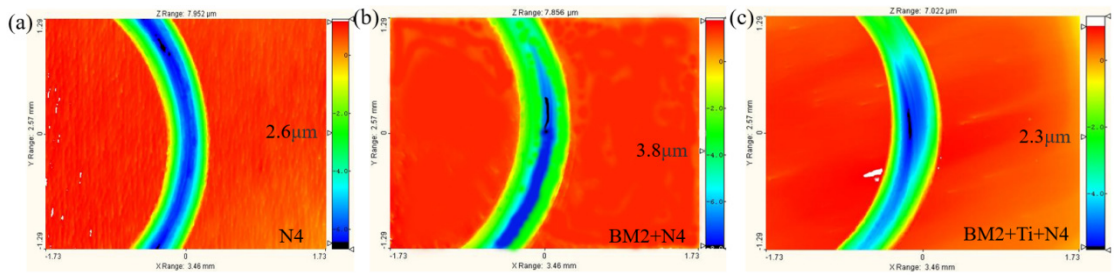

Figure 11. Cloud map of friction and wear depth distribution on the surface of nitrided layer: (a) N4; (b) BM2+N4; (c) BM2+Ti+N4.

Table 5. Friction and wear and nanoindentation performance parameters.

Sample	N4	BM2+N4	BM2+Ti+N4
Average wear depth (μm)	2.6±0.1	3.8±0.2	2.3±0.1
Wear rate (mm³/N·m)	$3.74\pm0.05\times10^{-8}$	$5.35\pm0.08\times10^{-8}$	$1.20\pm0.03\times10^{-8}$
Nanohardness (GPa)	5.1±0.3	5.1±0.5	5.4±0.3

4. Conclusions

(1) Pretreatment by introducing Ti particles via mechanical ball milling can construct Ti active sites on the surface of 42CrMo steel, and the Ti adhesion amount reaches 1.82±0.37 mg and tends to be saturated after 40 min of treatment. This pretreatment increases the total thickness of the gas nitrided layer at 520 °C for 4 h by 42.0% (from 20.8 μm to 29.5 μm) compared with the untreated sample, and controls the loose layer proportion at 16.9%, which is significantly better than pure ball milling pretreatment.

 doi:10.20944/preprints202605.1901.v1

(2) The hardness of the compact layer of the nitrided layer is stable at 648±3 HV, which is not affected by pretreatment; the introduction of Ti particles mainly improves the loose layer hardness, which rises stepwise from 525±3 HV to 560±2 HV, positively correlated with the surface content of TiN and TiO_2. The nanohardness increases from 5.1 GPa to 5.43 GPa, with an increase of about 5%–6%.

(3) The wear rate of BM2+Ti+N4 sample drops to 1.20×10^{-8} $mm^3/N\cdot m$, a reduction of 78% compared with the pure ball-milled sample. The wear mechanism changes from oxidative-adhesive wear to slight abrasive wear. The in-situ formation of the TiN compound layer fills surface micropores and strengthens the surface shear resistance, realizing the optimization of the wear resistance of the nitrided layer.

Author Contributions: Conceptualization: Jianhua Wang, Zhiwei Li; Methodology: Yulong Zhou, Hui Zhang, Yuan Yao, Yubo Zhang; Writing: Yulong Zhou, Zhiwei Li; Editing: Haoping Peng; Funding Acquistion: Jianhua Wang, Zhiwei Li.

Institutional Review Board Statement: Not applicable.

Informed Consent Statement: Not applicable.

Data Availability Statement: The authors confirm that the data supporting the findings of this study are available within the article.

Acknowledgments: Financial Support from the National Natural Science Foundation of China (52401076) and Research Start-up Fund of Changzhou University (ZMF23020196).

Conflicts of Interest: The authors declare no conflict of interest.

References

1. Chang X, Huang T, Yan Z, et al. Gas nitriding in the austenite region of pure iron: Effects of time and temperature[J]. Materials Today Communications, 2025, 43: 111560. https://doi.org/10.1016/j.mtcomm.2025.111560.
2. Yang G, Pan L, Deng J, et al. Effect of gas nitriding on microhardness and microstructure of laser cladding iron-based alloy coating[J]. Journal of Laser Applications, 2025, 37(2). https://doi.org/10.2351/7.0001749.
3. Feng Z, Wei K, Wang T, et al. Effect of laser scanning speed on the surface characteristics and wear resistance of TiZrAlV alloy via laser gas nitriding[J]. Surface and Coatings Technology, 2025, 500: 131909. https://doi.org/10.1016/j.surfcoat.2025.131909.
4. Kouba R, Rayane K, Keddam M. Thermodynamic reassessment of Fe-N and Fe-N-C systems. CALPHAD, 2020, 71: 102197. http://doi.org/10.1016/j.calphad.2020.102197.
5. Sharma P, Ju H, Figueiredo N M, et al. Exploring the potential of high-power impulse magnetron sputtering for nitride coatings: advances in properties and applications[J]. Coatings, 2025, 15(2): 130. https://doi.org/10.3390/coatings15020130.
6. Li C, Luo J, Zhao Z, et al. Effect of laser shock peening pretreatment on the microstructure and wear resistance of plasma nitrided TC4 Ti alloy[J]. Surface and Coatings Technology, 2025, 512: 132337. https://doi.org/10.1016/j.surfcoat.2025.132337.
7. Zhou H, Ma D, Dai L, et al. Mechanism study on the generation of oxygen vacancies by ball milling surface modification of siliceous minerals in coal gangue to enhance reactivity[J]. Applied Surface Science, 2025, 686: 162189. https://doi.org/10.1016/j.apsusc.2024.162189.
8. Qi Z, Zhang H, Guo X, et al. Preparation and Classification of Coatings by High-Energy Ball Milling: A Review[J]. Coatings, 2025, 15(11): 1343. https://doi.org/10.3390/coatings15111343.
9. Suvorova V S, Suvorov D S, Bochkanov F Y, et al. Improving surface properties of AlSi10Mg fabricated by cold spray: Mechanical milling is a tool for fabrication of composite ZrN/AlSi10Mg particles[J]. Advanced Engineering Materials, 2025, 27(4): 2401862. https://doi.org/10.1002/adem.202401862.

 doi:10.20944/preprints202605.1901.v1

10. Sunitha K, Vasudev H. A short note on the various thermal spray coating processes and effect of post-treatment on Ni-based coatings[J]. Materials Today: Proceedings, 2022, 50: 1452-1457. https://doi.org/10.1016/j.matpr.2021.09.017.
11. Zhizhong W, Chao H, Huang G, et al. Cold spray micro-defects and post-treatment technologies: a review[J]. Rapid Prototyping Journal, 2022, 28(2): 330-357. https://doi.org/10.1108/RPJ-12-2020-0302.
12. Kumar H, Singh A, Manikandan S G K, et al. Thermally-sprayed high-entropy alloy coating: mechanisms, properties and applications[M]//Powder Metallurgy. Woodhead Publishing, 2026: 177-205.https://doi.org/10.1016/B978-0-443-22025-8.00006-1
13. Provázková L, Olekšáková D, Kollár P, et al. Influence of mechanical milling intensity and powders surface treatment on energy losses of Fe compacts[J]. IEEE Transactions on Magnetics, 2026.https://doi.org/10.1109/TMAG.2026.3652020.
14. Wei L K, Abd Rahim S Z, Al Bakri Abdullah M M, et al. Producing metal powder from machining chips using ball milling process: A review[J]. Materials, 2023, 16(13): 4635. https://doi.org/10.3390/ma16134635.
15. Subhani T, Hafez K M, Khaliq A, et al. Microstructure characterization and intermetallic Fe-Al phases formation in Al2O3 nanoparticle-reinforced Al-20Sn-1Cu metal matrix nanocomposite coating on carbon steel[J]. Journal of the Indian Chemical Society, 2026: 102523. https://doi.org/10.1016/j.jics.2026.102523.
16. Liu Y, Liu YF, Zhang S, Zhang L, Zhang P, Zhang SR, Liu N. Structure characterization of the oxide film on FGH96 superalloy powders with various oxidation degrees[J]. Int J Min Met Mater, 2024, 31(9): 2037-2047. 10.1007/s12613-024-2823-x.
17. Mohammadi M, Akbari A, Warchomicka F, Pichon L. Depth profiling characterization of the nitride layers on gas nitrided commercially pure Ti[J]. Mater Charact, 2021, 181: 111453. https://doi.org/10.1016/j.matchar.2021.111453.
18. Gorin N, Akkus C S, Gramlich A, et al. Study of Nitrogen Diffusion in Aluminum Containing Plasma-Nitrided Air-Hardening Medium Manganese Steels[C]//EPJ Web of Conferences. EDP Sciences, 2026, 349: 01005. https://doi.org/10.1051/epjconf/202634901005.
19. Badamshin A M, Nesov S N, Kovivchak V S, et al. The influence of ion irradiation on the morphology and elemental and chemical composition of surface layers of tungsten-free hard alloys[J]. Technical Physics Letters, 2021, 47(10): 737-740. https://doi.org/10.1134/S1063785021080022.
20. Tao Y, Lin L, Ren X, et al. Duplex γ/α-phase evolution of biocompatible high-nitrogen stainless steel in additive manufacturing[J]. Journal of Materials Research and Technology, 2025.https://doi.org/10.1016/j.jmrt.2025.08.074.
21. Stabrawa I, Kubala-Kukuś A, Banaś D, et al. Characterization of the morphology of Ti and Ti (IV) oxide nanolayers deposited on different substrates by application of grazing incidence X-ray diffraction and X-ray reflectometry techniques[J]. Thin Solid Films, 2019, 671: 103-110.https://doi.org/10.1016/j.tsf.2018.12.034
22. Zhang Y, Peng Y, Wang A, et al. Impact toughness and strength synergy enabled by a stress-adaptive high-entropy alloy interlayer in laser-nitrided coatings[J]. Journal of Materials Research and Technology, 2025.https://doi.org/10.1016/j.jmrt.2025.11.082
23. Xia L, Li H, Feng H, et al. Enhanced strength and toughness of high nitrogen stainless bearing steel by controlling interstitial partitioning via V-microalloying[J]. Journal of Materials Science & Technology, 2023, 151: 204-218.https://doi.org/10.1016/j.jmst.2023.02.001
24. Hao X, Liu H, Zhang X, et al. Microstructure and wear resistance of in-situ TiN/(Nb, Ti) 5Si3 reinforced MoNbTaWTi-based refractory high entropy alloy composite coatings by laser cladding[J]. Applied Surface Science, 2023, 626: 157240.https://doi.org/10.1016/j.apsusc.2023.157240
25. Zhang P, Cheng Q, Yi G, et al. The microstructures and mechanical properties of martensite Ti and TiN phases in a Ti6Al4V laser-assisted nitriding layer[J]. Materials Characterization, 2021, 178: 111262. https://doi.org/10.1016/j.matchar.2021.111262
26. Liu D, Liu D, Wu Y, et al. Insight into nitriding behavior and corrosion mechanism in 17-4PH steel: The influence of nanocrystalline structure[J]. Journal of Materials Research and Technology, 2023, 27: 3761-3776. https://doi.org/10.1016/j.jmrt.2023.10.324

 doi:10.20944/preprints202605.1901.v1

27. Mahajan U, Dhonde M, Sahu K, et al. Ti nitride (TiN) as a promising alternative to plasmonic metals: a comprehensive review of synthesis and applications[J]. Materials Advances, 2024, 5(3): 846-895. https://doi.org/10.1039/D3MA00965C
28. Liu Y, Yang Y, Dong D, et al. Improving wear resistance of Zr-2.5 Nb alloy by formation of microtextured nitride layer produced via laser surface texturing/plasma nitriding technology[J]. Surfaces and Interfaces, 2020, 20: 100638. https://doi.org/10.1016/j.surfin.2020.100638